Document downloaded from:

http://hdl.handle.net/10251/165356

This paper must be cited as:

García-Hurtado, E.; Rodríguez-Fernández, A.; Moliner Marin, M.; Martínez, C. (2020). CO(2)hydrogenation using bifunctional catalysts based on K-promoted iron oxide and zeolite: influence of the zeolite structure and crystal size. Catalysis Science & Technology. 10(16):5648-5658. https://doi.org/10.1039/d0cy00712a

The final publication is available at

https://doi.org/10.1039/d0cy00712a

Copyright The Royal Society of Chemistry

Additional Information

CO_2 hydrogenation using bifunctional catalysts based on K-promoted iron oxide and zeolite: Influence of the zeolite structure and crystal size

Elisa García-Hurtado, Aída Rodríguez-Fernández, Manuel Moliner,* Cristina Martínez*

In the present manuscript, the influence of the zeolite structure and crystal size has been studied on bifunctional tandem catalysts combining K-promoted iron oxide (K/Fe_3O_4) with different zeolites for the CO_2 hydrogenation reaction at 320°C and 25 bar. First, to evaluate the influence of the zeolite structure on the CO_2 conversion, three different zeolite topologies have been evaluated (BEA, MFI and CHA) with similar Si/Al molar ratios. The combination of K/Fe_3O_4 with MFI maximizes the formation of aromatic products, while the combination with CHA and BEA increases the C_1-C_4 gas fraction, with high olefin selectivity. In addition, aromatics and aliphatic hydrocarbons are present in the condensed liquids of the tandem catalyst containing BEA, while no aromatics are observed for CHA. These different product selectivities can be ascribed to the different consecutive reactions within the three zeolites, where the MFI favors the aromatization of alkenes, and BEA and CHA favor oligomerization/cracking reactions leading to an increase of the light olefins yield. Second, the evaluation of the nanosized form of the three proposed zeolite frameworks has also been approached. The reduction of the particle size allows increasing the light olefins selectivity in all cases as compared to the zeolites with larger crystals. The shorter intracrystalline diffusional paths facilitate the egression of the light olefins before being involved in consecutive oligomerization reactions. In the particular case of the tandem catalyst with nanosized MFI zeolite, the C_2-C_4 fraction and its olefinicity are increased while maintaining the overall aromatic selectivity comparable to that obtained with the micron-sized MFI zeolites..

1. Introduction

Probably one of the most important commitments that our society must face is reducing greenhouse gas emissions, in particular CO_2, in order to diminish the global warming impact.[1] In this sense, many research efforts are being directed in the last years towards a progressive substitution of fossil fuels by renewable sources.[1–5] Among the different alternatives proposed, the use of CO_2 as raw material for the production of base chemicals or platform molecules is being intensively studied, since this can be theoretically considered as an interesting route towards a neutral carbon footprint.[6–8] However, the high thermodynamic stability and chemical inertness of the CO_2 molecule,[9] together with high kinetic barriers related to its participation in C-C formation reactions,[6,8] makes its direct conversion to hydrocarbons with more than two carbons (C_2^+) a major challenge.

CO_2 upgrading by thermochemical hydrogenation has received increasing attention, as its incorporation into synthetic gas streams for its conversion to hydrocarbons is a rather immediate alternative that can take advantage of the knowledge and technology associated with the Fischer-Tropsch Synthesis (FTS) process in the presence of conventional FTS catalysts.[7] The first evidences related to the CO_2 hydrogenation mechanism were reported back in the 80-90s.[10–13] In these early works, a two-step process was proposed, where CO_2 is first partially reduced to CO through the reverse water gas shift reaction (RWGSR) and hydrocarbons are formed in a second stage following the classical Fischer-Tropsch Synthesis (FTS) route.[12] Combination of the RWGSR, reversible and endothermic ($\Delta_R H_{300°C}$ = +38 kJ·mol^{-1}) with the FTS, which is an exothermic process ($\Delta_R H_{300°C}$ = +38 kJ·mol^{-1}), leads to an exothermic overall process.[8] Different metals and oxides were studied as catalysts for CO_2 hydrogenation, and those based on iron [14] and cobalt [15] were seen to be the most effective towards the formation of C_2^+ hydrocarbons. When converting classical syngas mixtures, Co is preferred as it favors high chain growth probabilities. However, when the feed is switched to H_2/CO_2 mixtures, Co leads to high methane selectivity while iron-based catalysts are more effective due to their ability for catalyzing the RWGSR in their oxidized form and for performing the FTS when fully carbidized.[8] The catalytic behavior of Fe-based FTS catalyst can be further improved by incorporating alkaline promoters that limit the production of undesired methane. K-promotion presents the additional benefit of enhancing carbidization of iron phases and increasing the selectivity to olefins and long-chain hydrocarbons.[12,16,17]

The FTS reaction is a polymerization process and, as such, it involves reactants' adsorption, chain initiation, and chain growth and termination steps.[18] The most accepted mechanisms are the CO-insertion and the carbide-type routes and their contribution to the overall process will be determined by the process conditions and the nature of the catalyst.[7] The type of active sites, the presence of promoters, process conditions or gas composition, among others [19–21] will also influence the FTS product distribution. In fact, a direct route to transform syngas into light olefins in the presence of supported iron catalysts has been described recently.[22] Still, conventional bulk promoted iron catalysts lead to a broad hydrocarbon spectrum, ranging from methane to C_{70+} following the Anderson–Schulz–Flory (ASF) distribution and, in those cases,

the use of bifunctional catalysts has been proposed for CO_2 upgrading to target products. These catalysts combine the metal oxide, able to activate CO_2 and to perform the FTS reaction, with an acid zeolite able to convert the FTS products into more valuable ones by means of consecutive reactions, such as hydrocracking, oligomerization, hydroisomerization or cyclization reactions.[23–25] Following this bifunctional approach, the product distribution will be determined by selecting the appropriate crystalline zeolite structure employed in these tandem catalysts. In this way, the formation of aromatic products or light olefins, for instance, may be favored by using medium-pore ZSM-5 (MFI structure) [26] or multipore mordenite (MOR structure) zeolites,[27] respectively.

It is well-known that controlling the textural properties of the zeolites and, in particular, reducing their crystal sizes to the nanometer scale (below 100 nm), can have a remarkable influence, not only on the catalytic activity of the zeolitic catalyst in terms of catalyst deactivation, but also on the product selectivities, which can be substantially altered.[28–30] Indeed, recently we have shown how the ability to decrease the particle size of well-known industrial zeolite-based catalysts, such as Beta or MFI, to particle sizes between 10-20 nm, has a direct impact on the product selectivity in complex reaction systems, such as the oligomerization of light olefins to liquid fuels, where enhancing the molecular diffusion of the bulky products is critical to control the final product selectivities,[31] or the methanol-to-olefin process, where activity was eight-fold higher and selectivity to ethylene and propylene was significantly increased.[32]

Herein, we propose the study of bifunctional tandem catalysts based on K-promoted iron oxide (K/Fe_3O_4) combined with three different zeolite structures, BEA, MFI and CHA, for the CO_2 hydrogenation reaction at 320°C and 25 bar. The three zeolites, with different topologies and pore openings (BEA, ~6.5-7 Å, pore system: 12x12x12; MFI, ~5.0-5.5 Å, pore system: 10x10x10; CHA, ~3.5 Å, pore system: 8x8x8) have been selected presenting similar Si/Al molar ratios (~10) with the aim of focusing the study on structural effects. The study of the K/Fe_3O_4 catalyst combined with the different zeolites reveals that the MFI maximizes the formation of aromatic products, whereas CHA and BEA convert the linear long-chain α-olefins obtained by the FTS catalyst increasing the proportion of hydrocarbons in the C_1-C_4 gas fraction, with high olefin selectivity. No aromatics are observed in the reaction products when using chabazite, but when K/Fe_3O_4 is combined with the large pore beta zeolite both, aromatic and aliphatic hydrocarbons, are detected in the condensed liquid fraction. Thus, the different zeolite pore topologies could maximize different consecutive reactions, being the activation of alkenes toward aromatics the favored reaction within MFI,[26,27] and oligomerization/cracking the main reactions taking place in the case of BEA and CHA, leading to a decrease of the C_5^+ hydrocarbon fraction and an increase of the light olefins yield.

Beyond studying the zeolite pore structure, the effect of decreasing the particle size into the nanometric scale of these three materials has also been approached. The enhanced accessibility of the large FTS products to the active sites achieved by decreasing the zeolite particle size is expected to modify the complex set of consecutive reactions taking place and will, therefore, have a significant influence on the product distribution. Indeed, the use of nanosized zeolites allows increasing the selectivity to light olefins in all cases as compared to standard zeolites with larger particle sizes, including MFI. This could be articulated as a result of the shorter diffusional paths in nanocrystalline zeolites that will facilitate the egression of these olefins out of the zeolite structure before getting involved in consecutive oligomerization reactions.

2. Experimental

2.1.- Synthesis

2.1.1.- Synthesis of K-promoted iron oxide (K/Fe_3O_4)

The K-promoted iron oxide was synthesized by modifying the procedure described in the literature.[26] 5.1 ml of an aqueous solution of hydrochloric acid (37%wt, Sigma-Aldrich) was added to 150 ml of MilliQ water. Then, 18.97 g of iron(III) chloride ($FeCl_3$, 97%, Sigma-Aldrich) and 8.00 g of iron(II) chloride ($FeCl_2$, 98%, Sigma-Aldrich) were added to the previous aqueous solution. The solution was heated to 60°C and, then, a 1.5 M aqueous solution of potassium hydroxide was added dropwise under stirring until achieving a pH~10. The mixture was kept under stirring for 1 hour. The precipitate was filtered and washed with 800 ml of distilled water. The solid was dried overnight at 60°C and directly used for CO_2 hydrogenation. ICP analysis reveals a ~1%wt of K in the final solid.

2.1.2.- Zeolite synthesis

The reference ZSM-5 (MFI) and beta (BEA) zeolites are commercially-available catalysts: MFI(10) and MFI(30) correspond to CBV2314 and CBV8020 materials, whereas BEA(10) corresponds to CP814E, all of them provided by Zeolyst. In the case of the CHA-type zeolite, CHA(10) has been prepared following a well-known recipe reported by Zones.[33]

The nanosized materials have been prepared following synthesis methods recently described by our group.[32,34] n-MFI(30) and n-BEA(10) zeolites have been synthesized using N-butyl-N-methylpyrrolidinium and N-butyl-N,N-dimethyl cyclohexylammonium as organic structure directing agents (OSDAs), respectively.[32] n-CHA(10) has been synthesized using FAU (CBV720, Si/Al~14, Zeolyst) and N,N,N-trimethyl-adamantammonium (TMAda, Sachem) as silicon source and OSDA, respectively.[34]

2.2.- Characterization

Powder X-ray diffraction (PXRD) measurements were performed with a multisample Philips X'Pert diffractometer equipped with a graphite monochromator, operating at 40 kV and 35 mA, and using Cu Kα radiation (λ = 0,1542 nm).

Chemical analyses were carried out in a Varian 715-ES ICP-Optical Emission spectrometer, after solid dissolution in HNO_3/HCl/HF aqueous solution. Elemental analyses were

Table 1 Chemical composition and textural properties of the materials studied as catalysts for the CO_2 hydrogenation

Sample	Pore topology	Si/Al	BET suf. area (m^2/g)	Microp. area (m^2/g)	External surf. area (m^2/g)	Microp. Vol. (cm^3/g)	Crystal size (nm)
BEA(10)	12x12x12	9.0	545	353	192	0.17	30-40
n-BEA(10)	12x12x12	14.4	717	405	312	0.18	10-15
MFI(10)	10x10x10	11.5	370	347	23	0.17	200
MFI(30)	10x10x10	30.9	389	343	46	0.17	200-300
n-MFI(30)	10x10x10	34.8	480	294	186	0.14	10-15
CHA(10)	8x8x8	9.3	628	587	40	0.28	200-300
n-CHA(10)	8x8x8	13.3	636	517	118	0.25	50-70

performed by combustion analysis using a Eurovector EA 3000 CHNS analyzer.

Textural properties were obtained from the N_2 adsorption-desorption isotherms measured at 77 K with a Micromeritics ASAP 2020 apparatus. The morphology of the samples was studied by field emission scanning electron microscopy (FESEM) using a ZEISS Ultra-55 microscope.

^{27}Al MAS NMR spectra were recorded at room temperature with a Bruker AV 400 MAS spectrometer at 104.2 MHz with a spinning rate of 10 kHz and 9° pulse length of 0.5 µs with a 1 s repetition time. ^{27}Al chemical shift was referred to $Al^{3+}(H_2O)_6$.

Infrared spectra were measured with a Nicolet 710 FT IR spectrometer. Pyridine adsorption-desorption experiments were made on self-supported wafers (10 $mg.cm^{-1}$) of original samples previously activated at 400°C and 10^{-2} Pa for 2 hours. After wafer activation, the base spectrum was recorded and pyridine vapor (6.5 10^2 Pa) was admitted in the vacuum IR cell and adsorbed onto the zeolite. Desorption of pyridine was performed under vacuum over three consecutive one-hour periods of heating at 150, 250 and 350°C, each of them followed by the IR measurement at room temperature. All the spectra were normalized to the area of the corresponding Si-O overtones (1755–2100 cm^{-1}). Values given for Brønsted and Lewis acid sites correspond to intensity of the IR bands at 1550 and 1450 cm^{-1}, respectively, given in arbitrary absorbance units (a.u.).

NH_3-TPD experiments were carried out in a Micromeritics 2900 apparatus. A calcined sample (100 mg) was activated by heating to 400°C for 2 h in an oxygen flow and for 2 h in argon flow. Subsequently, the samples were cooled down to 176°C, and NH_3 was adsorbed. The NH_3 desorption was monitored with a quadrupole mass spectrometer (Balzers, Thermo Star GSD 300T) while the temperature of the sample was ramped at 10°C min^{-1} in helium flow. Total ammonia adsorption was measured by repeated injection of calibrated amounts of ammonia at 100°C until saturation. Ammonia desorption was recorded by means of the mass 15, since this mass is less affected by the desorbed water.

2.3.- CO_2 hydrogenation catalytic test

CO_2 hydrogenation reactions were carried out in a Microactivity Effi reactor (PID Eng&Tech) equipped with a stainless-steel fixed bed reactor (9.1 mm ID). The catalysts were charged in the tubular reactor as a dual bed, with 0.5 g of K/Fe_3O_4 placed in the upper bed and 0.5 g of the corresponding zeolite in the lower bed. Both K/Fe_3O_4 and the zeolite are diluted with silicon carbide up to 1 cc and 2.5 cc, respectively, and the two beds are separated by 0.5 cc of silicon carbide. After catalysts activation by in-situ reduction at 350°C for 10 hours under 50 ml/min H_2 flow at atmospheric pressure, temperature was decreased to 320°C under 50 ml/min N_2 flow for reaction. Then, the reactant gas mixture $CO_2/H_2/N_2$ was fed, with a total flow of 242 ml/min (34 ml CO_2/200 ml H_2/8 ml N_2), resulting in a WHSV=7 h^{-1} (referred to K/Fe_3O_4) and a H_2/CO_2 molar ratio of 6. The final reaction pressure was set to 25 bar.

N_2, CO, CO_2 and C_1-C_6 hydrocarbons were analyzed on-line using a BRUKER 450 GC equipped with three independent channels. Hydrogen and permanent gases are separated with a Hayesep Q80 and molsieves 5A 80/100 and a 13X 80/100, respectively, and detected by two TCD. Hydrocarbons (C_1-C_6) are separated in an Al_2O_3/MAPD connected to a FID. The heavier hydrocarbons, condensed at the outlet of the reaction system, were analyzed off-line in a Shimatzu GC equipped with a HP-5 column connected to an FID and an MS by means of a detector splitting system. The carbon balances for all reactions were above 95%

3. Results

3.1.- Zeolite synthesis and characterization

Conversion of the long-chain hydrocarbons obtained by CO_2 hydrogenation through the RWGS and FTS reaction mechanisms in a consecutive zeolite bed will lead to different product distributions depending on the zeolite pore topology. Thus, three different zeolites have been considered with pore openings ranging from ~3.5 to ~6.5 Å, which are chabazite (CHA, ~3.5 Å), ZSM-5 (MFI, ~5.5 Å), and beta (BEA, ~6.5 Å). Beyond their different pore sizes, the three materials present crystalline frameworks with three-dimensional pore accessibility and large micropore volumes, parameters that could be determinant for enhancing, to different extents, the

complex set of consecutive reactions involving the FTS products. Interestingly, these three materials can be prepared with controlled chemical compositions, i.e. Si/Al molar ratios, and crystal sizes. Taking into account that Brønsted acidity of zeolites could be a critical factor for the consecutive reactions that can occur within the zeolite catalysts after the FTS step (i.e. oligomerization, cracking or isomerization, among others), the first set of zeolites selected present analogous Si/Al molar ratios (Si/Al~10). ZMS-5 and beta with Si/Al molar ratios of ~10 are commercially available zeolites, both materials provided by Zeolyst (CBV2314 and CP814E, respectively), and small-pore zeolite chabazite can be easily prepared following a well-known synthesis procedure reported by Dr. Stacey Zones.[33] These three materials have been named as BEA(10), MFI(10) and CHA(10).

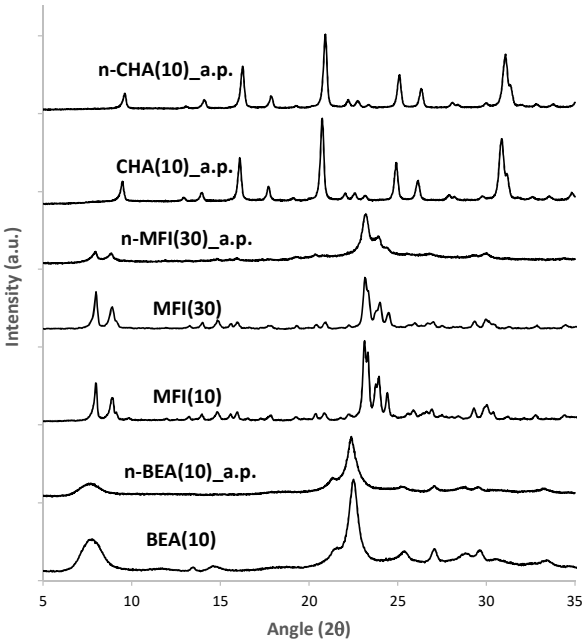

Fig. 1 PXRD patterns of the different zeolitic materials.

Their PXRD patterns show the characteristic diffractograms of BEA, MFI and CHA without the presence of impurity phases [see BEA(10), MFI(10) and CHA(10)_a.p. in Figure 1], and the chemical analyses reveal similar Si/Al molar ratios (~9-11, see Table 1). Their particle sizes have been evaluated by FE-SEM microscopy and, according to the images shown in Figure 2, MFI(10) and CHA(10) show analogous particles with average sizes of ~200-300 nm, whereas BEA(10) presents smaller particles formed by aggregated primary crystals of ~30-40 nm (see Figure 2). The N_2 adsorption experiments performed at 77 K indicate that the micropore volumes measured for these three materials are comparable to those reported in the literature, with ~0.17 cm^3/g for both BEA(10) and MFI(10), and ~0.28 cm^3/g for CHA(10) (see Table 1), revealing well-crystalline frameworks in all cases. As expected, BEA(10) presents a considerably higher external surface area (~190 m^2/g, see Table 1) than MFI(10) and CHA(10) (~20-40 m^2/g, see Table 1) as consequence of its smaller particle size. The nanosized counterparts of beta, ZSM-5 and chabazite have been prepared following recipes recently described in the literature.[32,34] The nanosized beta zeolite has been synthesized using N-butyl-N,N-dimethylcyclohexylammonium as OSDAs, and the solid obtained, with a final Si/Al molar ratio of ~13,[32] is a crystalline beta zeolite according to its PXRD pattern [see n-BEA(10) in Figure 1]. The crystal size of this material is ~10-15 nm [see n-BEA(10) in Figure 2], smaller than that of the commercial beta zeolite (~35-40 nm). This is in good agreement with their different textural properties, with the external surface area of the n-BEA(10) sample being 312 m^2/g, significantly larger than that of the commercial beta zeolite (192 m^2/g, see Table 1). It is worth noting that these differences in the crystal sizes of beta-type zeolites, apparently small, have been revealed crucial to improve the yields towards target products in diverse catalytic processes, such as olefin oligomerization or aromatic alkylation.[31,32,35]

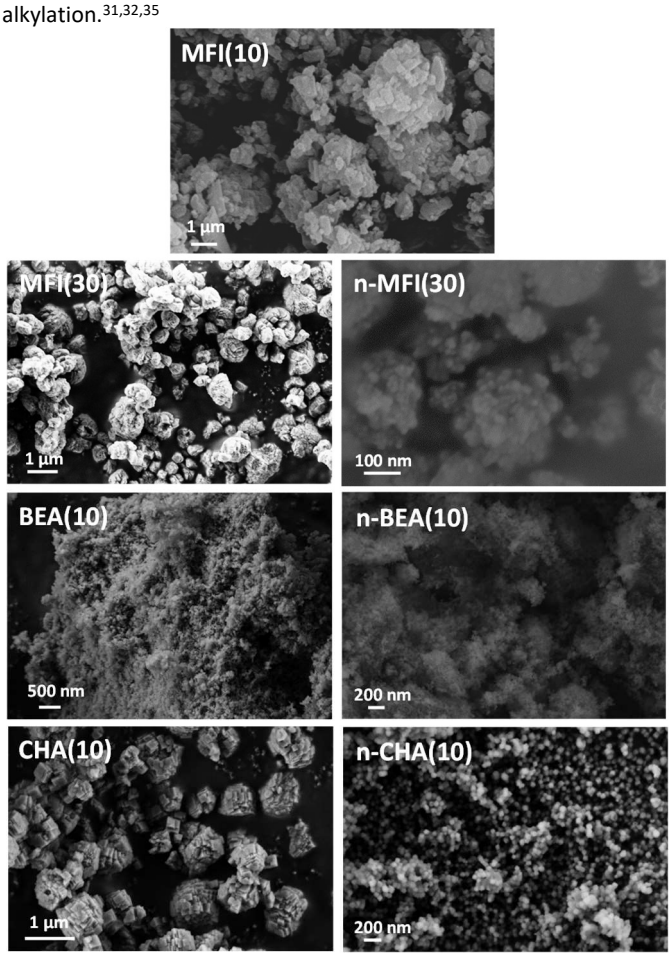

Fig. 2 FE-SEM images of the different zeolitic materials.

The nanosized MFI zeolite has been prepared with a Si/Al molar ratio of ~30 using N-butyl-N-methylpyrrolidinium as OSDA.[32] Since the Si/Al molar ratio of this material is higher than the one in the MFI(10) sample, an additional reference MFI zeolite with higher Si/Al molar ratio has been considered, MFI(30). The PXRD patterns of the MFI(30) and n-MFI(30) show the presence of the MFI structure in both materials, and the ICP analyses indicate similar Si/Al molar ratios (~31 and 35, respectively, see Table 1). FE-SEM images reveal different crystal sizes for MFI(30) and n-MFI(30), with average particles of 200-300 nm and 10-15 nm, respectively (see Figure 2 and Table 1), resulting in a considerably larger external surface area for the nanosized ZMS-5 zeolite (~186 m^2/g, see Table 1) as compared to standard MFI materials (~20-40 m^2/g, see Table 1).

Finally, the nanosized CHA zeolite has been prepared using TMAda as OSDA and high-silica FAU zeolite as initial silicon source.[34] The solid shows the characteristic PXRD pattern of CHA [see n-CHA(10) in Figure 1], and the measured Si/Al molar ratio is ~13 (see Table 1). The average crystal size of the n-CHA(10) sample is in the range of ~50-70 nm (see Figure 2), much smaller than that of the particles observed in the standard CHA zeolite (~200-300 nm, see CHA(10) in Figure 2).

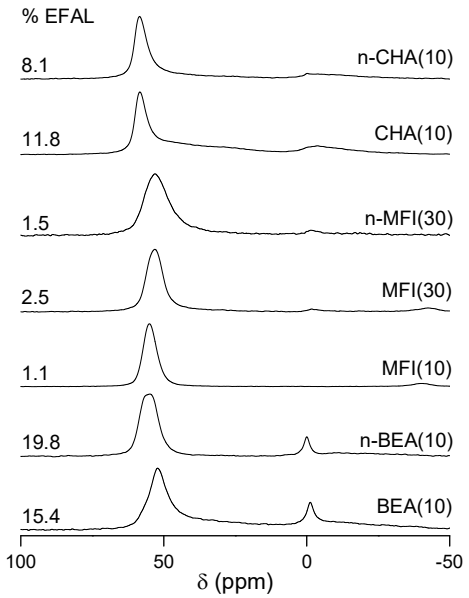

Fig. 3 ^{27}Al MAS NMR spectra of the different zeolitic materials in their acid form.

The different zeolites have been characterized by ^{27}Al MAS NMR to evaluate the aluminum coordination in the final acid solids. As shown in Figure 3, most of the aluminum species remain in tetrahedral coordination, as revealed by the more intense band centered at 50-55 ppm in the ^{27}Al MAS NMR spectra (see Figure 3). Still, a smaller band at 0 ppm indicates some octahedrally coordinated Al in extraframework positions (EFAL) is present in the case of the chabazites and the beta zeolites (~8 and 15-20%, respectively). The proportion of EFAL in these samples is comparable to values previously reported for nano-chabazites [34] and nano-betas.[32,35,36] The acidity of the MFI and BEA-type materials has been studied by IR spectroscopy combined with the adsorption of a base molecule, pyridine, and by evaluating the remaining amount of pyridine retained on the sites after subjecting the zeolite to increasing temperatures (250 and 350°C). The Brønsted and Lewis acid sites per gram of zeolite can be determined from the IR bands centered at 1545 and 1455 cm^{-1}, respectively (see Table 2 and Figure S1).[37] The MFI sample, with a Si/Al molar ratio of 10, presents higher Brønsted acid site density as compared to the MFI sample with a Si/Al molar ratio of 30, as could be expected from the higher Al content of the former. When comparing the two ZSM-5 zeolites with the highest Si/Al ratio, their acidity is similar, with the nanosized n-MFI(30) presenting slightly higher total acidity, and the reference MFI(30) slightly higher amount of Brønsted sites of medium-strong acidity. Regarding the two beta zeolites, the nanosized n-BEA(10) material show a higher total Brønsted acidity compared to BEA(10) (see Table 2), which could be explained by a larger amount of octahedrally-coordinated aluminum species in BEA(10). In good agreement with the ^{27}Al-NMR results, the amount of Lewis sites, related to cationic EFAL species, is significantly higher for the BEA samples than for the MFI zeolites, independently of the total Al content.

Table 2 Acidity of the BEA and MFI-type zeolites as determined by FT-IR combined with pyridine adsorption-desorption.

	Acidity (a.u)			
Sample	**Brønsted acid sites**		**Lewis acid sites**	
	T=250°C	T=350°C	T=250°C	T=350°C
BEA(10)	177	100	140	130
n-BEA(10)	280	171	196	173
MFI(10)	411	243	37	37
MFI(30)	127	101	28	28
n-MFI(30)	120	83	37	36

In the case of the CHA-type zeolites, the presence of the small pore windows mostly prevent the pyridine accessibility to the CHA cavities and, consequently, the Brønsted acidity of these materials has been evaluated by NH_3-TPD (see Figure S2). NH_3-TPD profiles show the presence of two desorption peaks for both CHA-type materials, where the low-temperature peak has been associated to weak interactions of physisorbed NH_3 (i.e. NH_3 adsorbed on octahedral Al sites) and the high-temperature peak has been assigned to the formation of NH_4^+ species at the Brønsted sites. Although CHA(10) shows a higher amount of weakly bounded NH_3 species than n-CHA(10) (see peaks between 100 and 300°C in Figure S2), fact that could be explained by the higher proportion of octahedral Al species in the former (see Figure 3), the amount of NH_4^+ species in the Brønsted sites is comparable for both materials (see peaks between 300 and 600°C in Figure S2). These results suggest a similar Brønsted acid site density for both CHA-type materials. The peak shifts observed towards lower temperatures for the n-CHA(10) sample could be ascribed to the shorter diffusion paths of the desorbed NH_3 within the nanosized CHA crystals. On the other hand, the decrease of the chabazite crystal size may result in a higher proportion of more external sites, probably less confined and, therefore, with reduced intrinsic acidity.[38]

3.2.- CO_2 hydrogenation reaction combining K/Fe_3O_4 with different standard zeolites (BEA, MFI and CHA)

First, the effect of the zeolite structure on the final hydrocarbon product distribution has been studied by combination of a K-promoted Fe_3O_4 with the different reference zeolites, all of them with a Si/Al molar ratio close to 10 [BEA(10), MFI(10) and CHA(10)]. The K/Fe_3O_4, synthesized following a recipe based on the one described by Wei et al.,[26] has been selected because K has been reported as an efficient promotor of iron-based FT catalysts, increasing the olefin selectivity within the FTs products.[12,39] The PXRD pattern of the starting K-promoted iron catalyst presents the diffractions characteristic of Fe_3O_4 (see Figure S3), a particle size of 10-15 nm (see Figure S4a-b), and the alkaline promoter is homogeneously dispersed (see Figure S4e). After the activation in H_2 atmosphere, the Fe_3O_4 phase is reduced to metallic iron, which is

converted in to a mixture of Fe_3O_4 and F_5C_2 when exposed to the H_2/CO_2 reaction atmosphere (see Figure S3), in good agreement with previous results.[26]

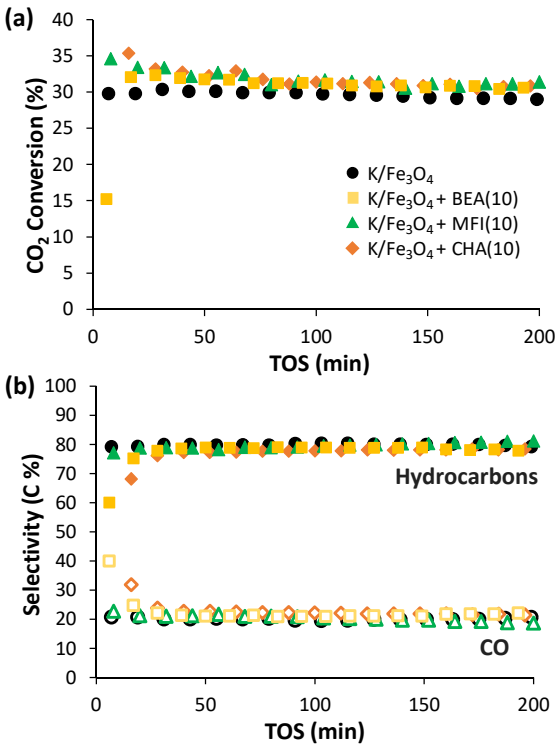

Fig. 4 CO_2 conversion (a) and overall product selectivity (b) to CO (open symbols) and hydrocarbons (solid symbols) with time-on-stream (TOS) catalyzed by K/Fe_3O_4 and combination of K/Fe_3O_4 with BEA(10), MFI(10) and CHA(10). Reaction conditions: 0.5 g K/Fe_3O_4, 0.5 g zeolite (if required), T=320°C, P=25 bar, H_2/CO_2 = 6 mol/mol, total flow = 142 ml/min (100 H_2/8 N_2/ 34 CO_2), WHSV=7 h^{-1} (referred to Fe_3O_4).

When K/Fe_3O_4 is used as sole catalyst for CO_2 hydrogenation at 350°C, 25 bar, WHSV=7 h^{-1} and a H_2/CO_2 molar ratio of 6, the CO_2 conversion obtained approaches 30% (see Figure 4a) with overall selectivity to CO and hydrocarbons around 20 and 80 C%, respectively (see Figure 4b). Among the hydrocarbon fraction, 39 and 61 C% correspond to the C_1-C_4 gases and C_5^+ products, respectively (see Figure 5). Methane, ethylene, propylene and 1-butene are the main products within this gas-fraction (see Figure 6a) and linear α-olefins predominate in the C_5^+ range (see Figure S5 and Table S1).

Combination of the FTS catalyst with the reference zeolites in a 1:1 weight ratio using a dual bed configuration (K/Fe_3O_4 : Zeolite, 0.5 g each), does not affect CO_2 conversion or overall selectivity to CO and hydrocarbons (see Figure 4). Indeed, CO_2 activation through RWGS and CO conversion through FTs are directly related to the K/Fe_3O_4 catalyst, and this explains the similar behavior of the three bifunctional systems. However, the presence of the zeolite in the downstream bed has a significant influence on the distribution of the hydrocarbon products, not only regarding their carbon number, but also according to the type of products obtained. Thus, the C_{5+} fraction is reduced, especially in the cases of beta and chabazite, in favor of an increased yield to C_1-C_4 gases (see Figures 5, 6 and S6).

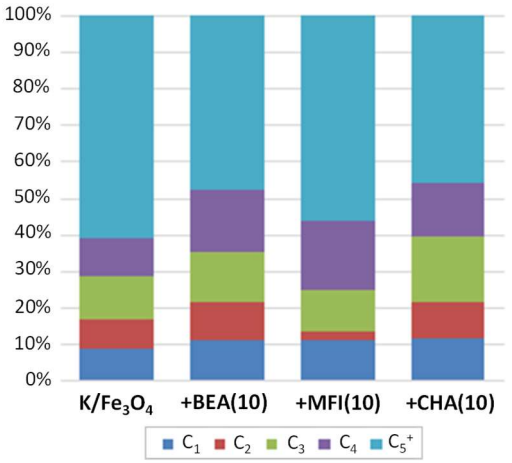

Fig. 5 Overall product distribution within the hydrocarbon fraction obtained with K/Fe_3O_4 and combination of K/Fe_3O_4 with BEA(10), MFI(10) and CHA(10). Reaction conditions: 0.5 g K/Fe_3O_4, 0.5 g zeolite (if required), T=320°C, P=25 bar, H_2/CO_2 = 6 mol/mol, total flow = 142 ml/min (100 H_2/8 N_2/ 34 CO_2), WHSV=7 h^{-1} (referred to Fe_3O_4).

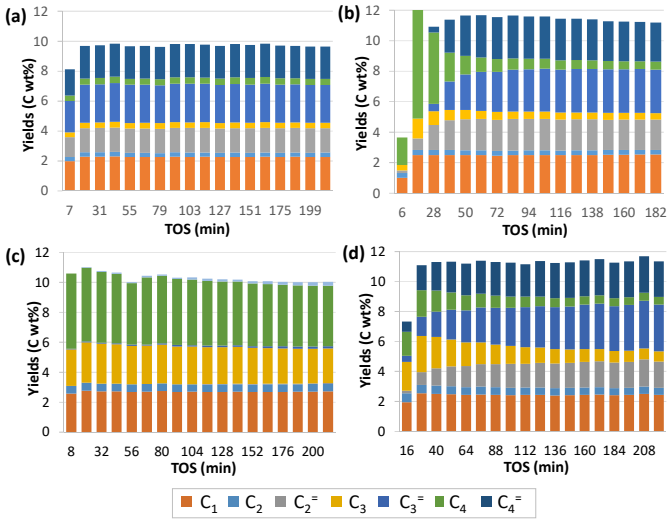

Fig. 6 Evolution of C_1-C_4 yields with TOS catalyzed by K/Fe_3O_4 (a) and combination of K/Fe_3O_4 with BEA(10) (b), MFI(10) (c) and CHA(10) (d). Reaction conditions: 0.5 g K/Fe_3O_4, 0.5 g zeolite (if required), T=320°C, P=25 bar, H_2/CO_2 = 6 mol/mol, total flow = 142 ml/min (100 H_2/8 N_2/ 34 CO_2), WHSV=7 h^{-1} (referred to Fe_3O_4).

In addition, BEA(10) increases ethylene and propylene as compared to the single K/Fe_3O_4 (see Figure 6), but it also increases the C_4 and C_5 products (see Table S1). 1-butene and 1-pentene are reduced in favor of 2-butenes, 2-pentenes and iso-olefins. Moreover, iso-butane and iso-pentane are formed in significant amounts (see Figure 6 and Table S1), two stable cracking products typically obtained by β-scission. The large 12-ring pores of the BEA structure will allow the access of a wide range of FTS products to the Brønsted acid sites located in the micropores, where they will undergo mainly cracking. In fact, only traces -if any- of the long chain α-olefins formed by the FTS catalyst are detected for the tandem K/Fe_3O_4+BEA(10) catalyst (see Figure S5), whereas part of the n-paraffins are still present in the condensed liquids. The primary cracking products may undergo consecutive reactions, such as re-cracking to lighter products, but also oligomerization and/or cyclization/aromatization, as evidenced by the presence of both, aliphatic and C_6-C_9 aromatic hydrocarbons

in the collected liquids. A closer look at the evolution with time on stream (TOS) of the C_1-C_4 fractions shows an induction period at short times on the production of light olefins, a period where an initially paraffin-rich C_3-C_4 fraction progresses towards a mixture formed mainly by olefins (see Figure 6b). Considering the high Al content of this beta zeolite with Si/Al molar ratio of 10, the low olefin/paraffin (O/P) ratios at short TOS can be explained by the high hydrogen transfer capacity of the fresh zeolite. The olefins present in the reaction media may oligomerize, cyclate and dehydrogenate leading to the formation of aromatics and/or coke. These aromatization reactions generally involve hydrogen transfer from the naphthenes to olefins, process that would explain the larger selectivity to light alkanes at short TOS (see Figure 6b). Although in a significantly lower extension, recent findings suggest that direct hydrogenation of part of the olefins under the H_2 pressure conditions used in this work cannot be discarded.[40] In any case, after the first hour on stream, the composition of the mixture is stabilized at high O/P ratios zeolite, close to those obtained with the K/Fe_3O_4 catalyst alone (see Figure S7a), probably due to partial deactivation of the zeolite. It is important to note that at longer TOS, under steady state conditions, the absolute yield to $C_2^=$-$C_4^=$ olefins is increased by the presence of the beta zeolite (see Figure S7b), indicating that its cracking capacity is maintained during the whole experiment.

Combination of the K/Fe_3O_4 catalyst with the small pore chabazite, CHA(10), increases mainly the C_3 fraction (see Figure 5). In this case, the 8-ring pore channel system will enable the conversion of the C_5 and C_6 FTS products, but larger hydrocarbons will be converted mainly on the external surface or at the pore mouths of the zeolite due to sterical hinderance and diffusional problems.[41,42] It is interesting how the small pore crystalline structure limits formation of isobutene and isobutane, resulting in an increase of the C_2 and C_3 fractions (see Table S1).[43] However, the high Al content of this zeolite results in the formation of ethane and propane during the initial stages of the reaction (see Figure 6d), due to hydrogen transfer reactions, especially favored within the cavities of the CHA structure. As in the case of combination of the FTS catalyst with zeolite beta, the presence of chabazite results in total conversion of the α-olefins (see Figure S5). However, no aromatic hydrocarbons are observed in this case (see Figure S5), because due to the small dimension of the 8-ring channels, the aromatics that may be formed within the CHA cavities will not be able to diffuse out of these cages.

The results obtained with the tandem catalyst K/Fe_3O_4+MFI(10) are completely different from the two cases described so far. The first thing to the noted is that the C_5^+ fraction is only slightly reduced as compared to FTS catalyst alone, although within the gases the C_2 fraction is significantly smaller, whereas C_4 hydrocarbons are formed in a larger proportion (see Figure 5). Moreover, the olefinicity in the C_2 to C_4 fraction is very low (see Figures 6c, S6c and S7), and mainly paraffins are obtained. This is in good agreement with the composition of the C_5^+ fraction shown in Figure S8, formed mainly by aromatic hydrocarbons belonging to the BTX fraction (96%, see Table S2, which makes a selectivity of 43 % in the overall hydrocarbon range). In fact, the ability to transform FTS products within the medium pore MFI pore system through cyclization-aromatization reactions has been proposed as the most plausible reaction mechanism leading to an enhancement of the selectivity to aromatics.[26,27]

These preliminary results on combining different standard zeolite structures with a well-stablished iron-based FTS catalyst undoubtedly highlight the importance of the zeolite framework topology on guiding the product selectivity towards different target products starting from CO_2 as initial source. The fine-tuned control of the complex secondary reaction set occurring within the different zeolite pore systems will be critical for maximizing the selectivity towards the desired products. In this sense, controlling the crystal size of these zeolite frameworks will enhance the accessibility of the FTS products to the inner structure of the zeolite particles but may also increase the secondary reactions that can occur on the external surface of the zeolite crystals or in the pore mouths. Considering this, the catalytic evaluation of nanosized zeolites in combination with K/Fe_3O_4 has been explored.

3.3.- CO_2 hydrogenation reaction combining K/Fe_3O_4 with different nanosized zeolites (BEA, MFI and CHA)

MFI(10) has been shown as a very efficient component in the dual bed catalyst to guide the transformation of the FTs products coming from the K/Fe_3O_4 bed into BTX aromatic molecules. However, if the product distribution in the gases is analyzed, it can be observed that this ZSM-5 with a Si/Al=10 and, consequently, a high Brønsted acid site density, has a poor ability to allow the formation of light olefins (see Figures 6c, S6c and S7), with a $C_{2=}$-$C_{4=}$ selectivity of 1.0 C% considering the total hydrocarbon range (see Table S1), due to aromatization following the hydrogen transfer mechanism.

A recent study shows that it is possible to convert syngas to hydrocarbons with high aromatic selectivity and limited formation of light alkanes in the presence of tandem FTS+HZSM-5.[44] This is achieved by controlling the amount of zeolite downstream of the FTS catalyst, so that the FTS olefins are aromatized by a direct dehydrogenation mechanism and not by means of the hydrogen transfer pathway. Extrapolating this to our catalytic system, lower Al contents and, therefore, a lower amount of Brønsted acid sites in our MFI zeolite, will reduce the extension of bimolecular hydrogen transfer reactions improving the selectivity towards light alkenes. Moreover, reducing the size of the zeolite crystals will also favor the diffusion of primary products without them being involved in undesired secondary reactions, and this may also result in a higher olefinicity of the C_2-C_4 gases. Recently, we have described the synthesis of the nanosized high-silica MFI zeolite with average particle sizes between 10-15 nm using very simple OSDA molecules.[32] The optimized nanosized MFI zeolite following this simple methodology presents a Si/Al molar ratio of ~30, n-MI(30), with a significantly reduced Brønsted acid site density as compared to MFI(10) [see n-MFI(30) in Table 1]. In order to evaluate, independently, influence of the crystal size, the catalytic evaluation of a tandem catalyst presenting a standard MFI zeolite with a similar Si/Al ratio is included for fair comparisons [see physico-chemical properties of MFI(30) in Tables 1 and 2].

Increasing the Si/Al molar ratio of the MFI component in the bifunctional catalysts from 10 to 30 leads to an important decrease of the total amount of Brønsted acid sites (see Table 1). Although this, as could be expected, does not affect the overall selectivity to CO and hydrocarbons (see Figure S8), it results in a lower cracking activity of MFI(30) and, consequently, in a lower proportion of light C_1-C_4 hydrocarbons and an increase of the C_5^+ hydrocarbons (see

Figure 7a) as compared to MFI(10). Still, when analyzing the composition of the condensed products, more than 90 % are aromatic hydrocarbons (see Figure S9 and Table S2) and the selectivity to aromatics within the hydrocarbon fraction is 45%, similar to the one obtained with MFI(10), of 43%. The main difference as compared to MFI(10) is that a broader spectrum of aromatic products is formed, which includes C_9 and C_{10}^+ aromatics (see Table S2). Thus, the fraction of BTX in aromatics obtained with MFI(10) and MFI(30) decreases from 96 to 85% (see Table S2) due to the lower cracking and dealkylation capacity of the ZSM-5 with higher Si/Al ratio. Regarding the gas fraction, the yields to ethane, propane and butanes are reduced when decreasing the Al content of ZSM-5 (see Figure 8a, Figure S10a and Table S1), but no significant differences are observed regarding the olefinicity of the C_2-C_4 fraction (see Figure 7b).

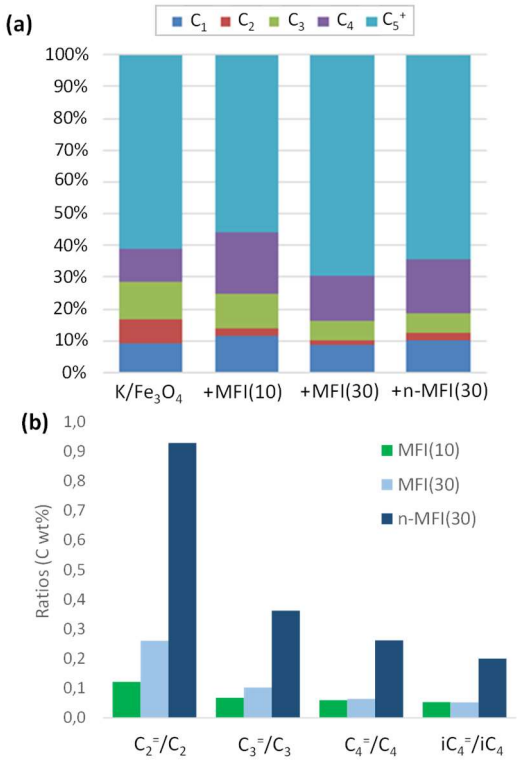

Fig. 7 Overall product distribution within the hydrocarbon fraction (a) and olefin to paraffin ratios in C_2-C_4 (b) obtained with K/Fe_3O_4 and combination of K/Fe_3O_4 with MFI(10), MFI(30) and n-MFI(30). Reaction conditions: 0.5 g K/Fe_3O_4, 0.5 g zeolite (if required), T=320°C, P=25 bar, H_2/CO_2 = 6 mol/mol, total flow = 142 ml/min (100 H_2/8 N_2/ 34 CO_2), WHSV=7 h^{-1} (referred to Fe_3O_4).

When combining K/Fe_3O_4 with nanocrystalline n-MFI(30), we observe a reduction of the C_5^+ fraction as compared to the micron-sized ZSM-5 with comparable Al content (see Figure 7a) in favor of a higher selectivity to C_2 and C_4. The higher external surface area of the nano-zeolite and the shorter diffusion path lengths will facilitate the access and conversion of the long-chain hydrocarbons formed on the K/Fe_3O_4 catalyst. The aromatic content within the condensed fraction is still close to 90%, and the overall aromatic selectivity in hydrocarbons is 41%, in the range as that obtained with the micronsized MFI(10) and MFI(30), of 43 and 45%, respectively. The larger external surface area shifts the aromatic distribution to higher proportions of heavier C_9^+ aromatics, but the selectivity to the desired BTX is still high (76.1%, see Table S2), and the heavy aromatics can be easily transformed into the more valuable BTX by means of well-known transalkylation processes.[45,46] It is interesting to note that, as expected, the selectivity to light olefins has been increased when combining the FTS catalyst with the nano-ZSM-5 n-MFI(30) (see Figure 7b). Thus, the incorporation of the nanosized MFI material into the bifunctional catalytic system with K/Fe_3O_4, not only maintains a high selectivity towards aromatic products, but also allows an increase of the overall selectivity to light olefins as compared to the standard MFI zeolites.

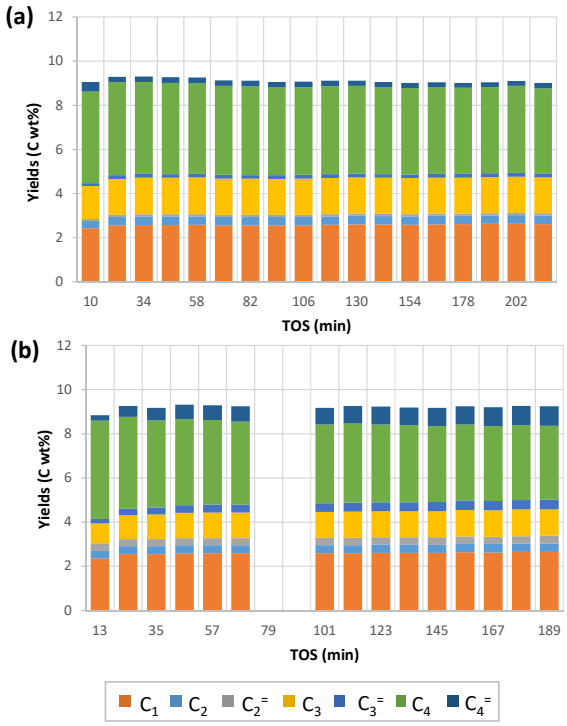

Fig. 8 Evolution of C_1-C_4 yields with TOS catalyzed by K/Fe_3O_4 in combination with MFI(30) and n-MFI(30) (b). Reaction conditions: 0.5 g K/Fe_3O_4, 0.5 g zeolite, T=320°C, P=25 bar, H_2/CO_2 = 6 mol/mol, total flow = 142 ml/min (100 H_2/8 N_2/ 34 CO_2), WHSV=7 h^{-1} (referred to Fe_3O_4).

Reducing the ZSM-5 crystal size and increasing the accessibility to the active sites, close to the external surface and/or pore mouths of the MFI zeolite nanoparticles, has been shown to enhance cracking/oligomerization reactions of the long-chain linear a-olefins obtained on the FTS catalysts, and a similar trend could be expected for the other two zeolite structures proposed in this work, BEA and CHA. As stated above, nanosized high-silica beta and chabazite zeolites with average particle sizes of 10-15 and 50-70 nm, respectively, can be prepared following simple synthesis methods [see physico-chemical properties of n-BEA(10) and n-CHA(10) in Tables 1 and 2].[32,34]

When combining these two nanosized materials with the K-promoted iron oxide, the overall selectivity to CO and hydrocarbons is maintained as compared to that obtained with the corresponding micron-sized reference zeolites (see Figure S11). However, reduction of the crystal size to the nano-range has a clear effect in the product distribution within the hydrocarbon fraction. In the case of the large

pore beta zeolites, the n-BEA(10) enhances the conversion of the FTS products as evidenced by a decrease of the C_5^+ fraction (see Figure 9a), especially of the C_6^+ fraction (see Table S1) and an enhanced formation of C_4 hydrocarbons as compared to reference BEA(10). This could be due to a reduced extension of C_4 oligomerization reactions due to the shorter residence time of these cracking products within the shorter pores of the nanocrystals, despite the larger amount of total Brønsted acid sites of the nanosized beta. Regarding the selectivity within the gases, although the final values obtained after 2 hours on stream for both beta zeolites are comparable, they show different C_1-C_4 profiles at shorter times, particularly for light olefins (see Figure 10a-b and S12a-b). Indeed, n-BEA(10) requires longer TOS to achieve the steady-state production of $C_{2=}$-$C_{4=}$ as compared to standard Beta(10) (see Figure S12a-b). As observed previously for other processes,[31,35] the smaller dimensions of the crystals will delay the partial deactivation of the nano-zeolite and a larger amount of acid sites will be available for longer times contributing to hydrogen transfer reactions.

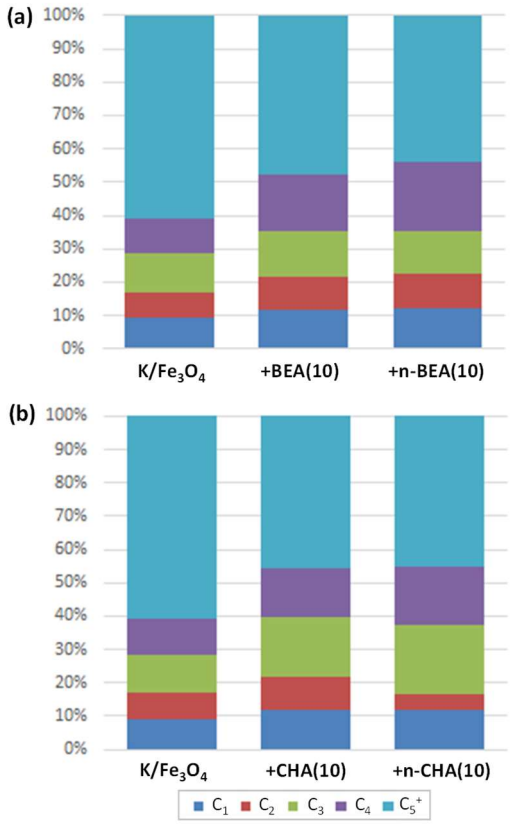

Fig. 9 Overall product distribution within the hydrocarbon fraction obtained with catalyst K/Fe_3O_4 and combination of K/Fe_3O_4 with BEA(10) and n-BEA(10) (a) and K/Fe_3O_4 and combination of K/Fe_3O_4 with CHA(10) and n-CHA(10) (b). Reaction conditions: 0.5 g K/Fe_3O_4, 0.5 g zeolite, T=320°C, P=25 bar, H_2/CO_2 = 6 mol/mol, total flow = 142 ml/min (100 H_2/8 N_2/ 34 CO_2), WHSV=7 h^{-1} (referred to Fe_3O_4).

When looking at the hydrocarbon distribution obtained for the reference and nano-chabazite zeolites (see Figure 9b), the C_5^+ fraction is comparable, but there is a clear difference in the selectivity within the C_1-C_4 gases. Indeed, the propylene yield under steady state conditions is increased from 3 to 4 C%, which results in an increase in selectivity from ~11 to ~14 C% within the C_1-C_4 fraction (see Figures 10c-d and S12c-d). The selectivity to butenes, although in a lower extent, is also increased. As in the case of the BEA zeolites, a decrease in the crystal size of CHA increases the length of the induction period where n-paraffins predominate within the C_1-C_4 fraction. Again, a delayed partial deactivation may be the explanation for this behavior. Moreover, the larger difference in crystal sizes when comparing CHA(10) and n-CHA(10) makes the increase in the induction period more evident than in the case of the beta zeolites.

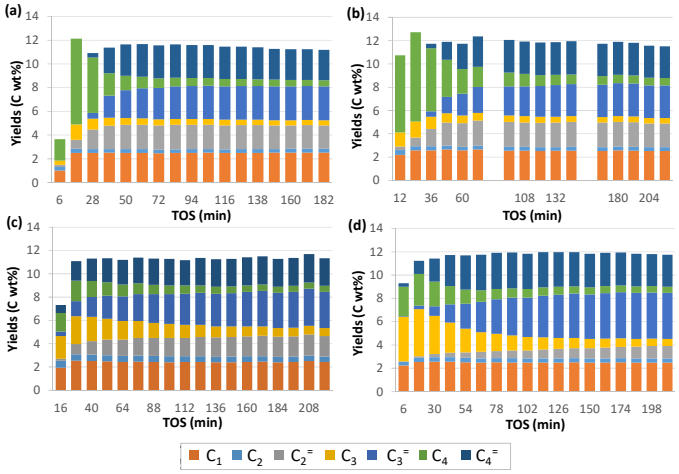

Fig. 10 Evolution of C_1-C_4 yields with TOS catalyzed by K/Fe_3O_4 in combination with BEA(10) (a), n-BEA (10), CHA(10) (c) and n-CHA(10) (d). Reaction conditions: 0.5 g K/Fe_3O_4, 0.5 g zeolite, T=320°C, P=25 bar, H_2/CO_2 = 6 mol/mol, total flow = 142 ml/min (100 H_2/8 N_2/ 34 CO_2), WHSV=7 h^{-1} (referred to Fe_3O_4).

Summarizing, the combination of K/Fe_3O_4 with nano-crystalline zeolites allows increasing the conversion of the long-chain FTS products into valuable chemicals. In the case of ZSM-5, reducing the crystal size results in an increase of the olefin selectivity within the gases while maintaining high selectivity towards aromatic hydrocarbons. Regarding beta and chabazite, the former increases the selectivity to the C_2-C_4 fraction without changing significantly the distribution within the gases, but, in contrast, n-CHA(10) improves significantly the selectivity to propylene as compared to the reference zeolite.

4.- Conclusions

This work studies the influence of zeolite structure and crystal size on the conversion of CO_2 on multifunctional catalysts combining K/Fe_3O_4 with different zeolites. Zeolites with three different topologies have been compared, BEA, MFI, and CHA. As expected, addition of the zeolite in a separate bed downstream of the FTS catalysts does not affect CO_2 conversion nor the overall selectivity to CO and hydrocarbons. However, hydrocarbon distribution is strongly influenced by the zeolite structure. Thus, chabazite and beta convert the linear α-olefins obtained on the FTS catalysts into lighter products, reducing significantly the C_5^+ fraction and increasing the C_1-C_4 selectivity. Under steady state conditions, the olefinicity of the C_2-C_4 fraction is very high, with olefin to paraffin ratios comparable to those obtained with the FTS catalyst alone, but with increased yields to ethylene, propylene and butenes. On the other hand, MFI

increases yield to C_{5}^{+} hydrocarbons, but converting the FTS products into aromatics, mainly in the BTX fraction.

When the nano-crystalline zeolites are combined with K/Fe_3O_4, the conversion of the long-chain FTS products into valuable chemicals is further enhanced, and higher yields to light olefins are obtained for the tandem catalysts containing beta and chabazite. Olefinicity of the C_2-C_4 fraction is also increased when the K/Fe_3O_4 is combined with the nano-sized ZSM-5, while maintaining an overall aromatic selectivity in hydrocarbons in the range of that obtained with the micronsized MFI zeolites.

Acknowledgements

This work has been supported by Spanish Government through ''Severo Ochoa" (SEV-2016-0683, MINECO) and RTI2018-101033-B-I00 (MCIU/AEI/FEDER, UE), by the Fundación Ramón Areces through a research contract (CIVP18A3908) and by Generalitat Valenciana (AICO/2019/060). A.R.F. acknowledges the Spanish Government-MINECO for a FPU scholarship (FPU2017/01521). The Electron Microscopy Service of the UPV is acknowledged for their help in sample characterization.

Notes and references

1 M. Höök and X. Tang, *Energy Policy*, 2013, **52**, 797–809.
2 I. Dincer, *Renew. Sustain. Energy Rev.*, 2000, **4**, 157–175.
3 N. Kannan and D. Vakeesan, *Renew. Sustain. Energy Rev.*, 2016, **62**, 1092–1105.
4 A. Corma, S. Iborra and A. Velty, *Chem. Rev.*, 2007, **107**, 2411–2502.
5 S. Abate, K. Barbera, G. Centi, P. Lanzafame and S. Perathoner, *Catal. Sci. Technol.*, 2016, **6**, 2485–2501.
6 A. Goeppert, M. Czaun, J.-P. Jones, G. K. Surya Prakash and G. A. Olah, *Chem. Soc. Rev.*, 2014, **43**, 7995–8048.
7 G. Prieto, *ChemSusChem*, 2017, **10**, 1056–1070.
8 R. W. Dorner, D. R. Hardy, F. W. Williams and H. D. Willauer, *Energy Environ. Sci.*, 2010, **3**, 884.
9 P. Gao, S. Li, X. Bu, S. Dang, Z. Liu, H. Wang, L. Zhong, M. Qiu, C. Yang, J. Cai, W. Wei and Y. Sun, *Nat. Chem.*, 2017, **9**, 1019–1024.
10 G. D. Weatherbee and C. H. Bartholomew, *J. Catal.*, 1984, **87**, 352–362.
11 M.-D. Lee, J.-F. Lee, C.-S. Chang and T.-Y. Dong, *Appl. Catal.*, 1991, **72**, 267–281.
12 J. Lee, W. Chern, M. Lee and T. Dong, *Can. J. Chem. Eng.*, 1992, **70**, 511–515.
13 D. Jean-Luc, S. Kazuhiro and A. Hironori, *Chem. Lett.*, 1992, **21**, 5–8.
14 M. Pijolat, V. Perrichon, M. Primet and P. Bussiere, *J. Mol. Catal.*, 1982, **17**, 367–380.
15 A. Guerrero-Ruiz and I. Rodríguez-Ramos, *React. Kinet. Catal. Lett.*, 1985, **29**, 93–99.
16 H. Jahangiri, J. Bennett, P. Mahjoubi, K. Wilson and S. Gu, *Catal. Sci. Technol.*, 2014, **4**, 2210–2229.
17 A. Ramirez, L. Gevers, A. Bavykina, S. Ould-Chikh and J. Gascon, *ACS Catal.*, 2018, **8**, 9174–9182.
18 R. B. Anderson, R. A. Friedel and H. H. Storch, *J. Chem. Phys.*, 1951, **19**, 313–319.
19 A. Griboval-Constant, A. Butel, V. V. Ordomsky, P. A. Chernavskii and A. Y. Khodakov, *Appl. Catal. A Gen.*, 2014, **481**, 116–126.
20 J. Patzlaff, Y. Liu, C. Graffmann and J. Gaube, *Appl. Catal. A Gen.*, 1999, **186**, 109–119.
21 J. Patzlaff, Y. Liu, C. Graffmann and J. Gaube, *Catal. Today*, 2002, **71**, 381–394.
22 H. M. Torres Galvis, J. H. Bitter, C. B. Khare, M. Ruitenbeek, A. I. Dugulan and K. P. de Jong, *Science*, 2012, **335**, 835–838.
23 H. Kim, D.-H. Choi, S.-S. Nam, M.-J. Choi and K.-W. Lee, in *Stud. Surf. Sci. Catal.*, 1998, pp. 407–410.
24 S.-S. Nam, H. Kim, G. Kishan, M.-J. Choi and K.-W. Lee, *Appl. Catal. A Gen.*, 1999, **179**, 155–163.
25 A. Dokania, A. Ramirez, A. Bavykina and J. Gascon, *ACS Energy Lett.*, 2019, **4**, 167–176.
26 J. Wei, Q. Ge, R. Yao, Z. Wen, C. Fang, L. Guo, H. Xu and J. Sun, *Nat. Commun.*, 2017, **8**, 15174.
27 A. Ramirez, A. Dutta Chowdhury, A. Dokania, P. Cnudde, M. Caglayan, I. Yarulina, E. Abou-Hamad, L. Gevers, S. Ould-Chikh, K. De Wispelaere, V. van Speybroeck and J. Gascon, *ACS Catal.*, 2019, **9**, 6320–6334.
28 S. Mintova, J.-P. Gilson and V. Valtchev, *Nanoscale*, 2013, **5**, 6693.
29 S. Mintova, M. Jaber and V. Valtchev, *Chem. Soc. Rev.*, 2015, **44**, 7207–7233.
30 J. D. Rimer, M. Kumar, R. Li, A. I. Lupulescu and M. D. Oleksiak, *Catal. Sci. Technol.*, 2014, **4**, 3762–3771.
31 M. R. Díaz-Rey, C. Paris, R. Martínez-Franco, M. Moliner, C. Martínez and A. Corma, *ACS Catal.*, 2017, **7**, 6170–6178.
32 E. M. Gallego, C. Paris, M. R. Díaz-Rey, M. E. Martínez-Armero, J. Martínez-Triguero, C. Martínez, M. Moliner and A. Corma, *Chem. Sci.*, 2017, **8**, 8138–8149.
33 US4544538A, 1985.
34 E. M. Gallego, C. Li, C. Paris, N. Martín, J. Martínez-Triguero, M. Boronat, M. Moliner and A. Corma, *Chem. Eur. J.*, 2018, **24**, 14631–14635.
35 R. Martínez-Franco, C. Paris, M. E. Martínez-Armero, C. Martínez, M. Moliner and A. Corma, *Chem. Sci.*, 2016, **7**, 102–108.
36 M. A. Camblor, A. Corma and S. Valencia, *Microporous Mesoporous Mater.*, 1998, **25**, 59–74.
37 C. A. Emeis, *J. Catal.*, 1993, **141**, 347–354.
38 M. Boronat and A. Corma, *ACS Catal.*, 2019, **9**, 1539–1548.
39 A. Ramirez, S. Ould-Chikh, L. Gevers, A. D. Chowdhury, E. Abou-Hamad, A. Aguilar-Tapia, J. Hazemann, N. Wehbe, A. J. Al Abdulghani, S. M. Kozlov, L. Cavallo and J. Gascon, *ChemCatChem*, 2019, **11**, 2879–2886.
40 S. S. Arora, Z. Shi and A. Bhan, *ACS Catal.*, 2019, **9**, 6407–6414.
41 M. Dusselier and M. E. Davis, *Chem. Rev.*, 2018, **118**, 5265–5329.
42 M. Moliner, C. Martínez and A. Corma, *Chem. Mater.*, 2014, **26**, 246–258.
43 X. Tang, H. Zhou, W. Qian, D. Wang, Y. Jin and F. Wei,

Catal. Letters, 2008, **125**, 380–385.
44 J. L. Weber, I. Dugulan, P. E. de Jongh and K. P. de Jong, *ChemCatChem*, 2018, **10**, 1107–1112.
45 W. Vermeiren and J.-P. Gilson, *Top. Catal.*, 2009, **52**, 1131–1161.
46 T. Tsai, *Appl. Catal. A Gen.*, 1999, **181**, 355–398.